Chapter 6

Segmentation and Classification of Large Regions

The work presented in this chapter consists of two parts.

The aim of the first part was to develop a region-based segmentation of the SAR image. The purpose of such a segmentation is to find uniform regions in the image. This segmentation can then be either used as a starting point for a classification, used in the development of specific detectors or used to improve the segmentation results offered by the edge detection. The segmentation is discussed in the next section.

The second idea explored here was to directly classify the SAR image to find main classes that are likely to be present on maps (e.g. forests, agricultural areas, villages,...). The approach presented here is based on decomposition methods. Decomposition methods convert the polarimetric information into information about the scattering properties of the terrain. If these scattering properties can be linked to physical properties of different lancovers, this results in an unsupervised classification method.

6.1 Image Segmentation using Merging Methods

In optical images the observed image is usually close to the ideal image; it is only corrupted by additive noise, usually according to an approximately Gaussian noise model with high signal to noise ratio. Therefore segmentation techniques can be developed that are based on measurements of local intensity (e.g. thresholding methods). Only in case of textured regions larger neighbourhoods need to be considered in the segmentation. As mentioned before, in SAR images, the noise-like characteristics of the speckle cause classical segmentation methods to fail. Especially methods based on measurements of local intensity will not be suited for SAR. The only way to take into account the large point-to-point variations due to speckle is to consider the statistics of the image in the neighbourhood of the current pixel.

In [24] a segmentation based on a clustering method for multi-look polarimetric SAR images is proposed. The clustering is based on the elements of the polarimetric covariance matrix and assumes azimuthal symmetry. Required input parameters are the number of clusters, the maximum separation between clusters and the maximal cluster size. In [25] the method is adapted and the number of clusters is determined automatically within a

range of possible values. Clustering methods thus usually require some user input (a range of possible numbers of clusters). They are not completely unsupervised.

An alternative is offered by region growing methods [42]. The idea is to start with an over-segmented image and to fuse neighbouring regions if they satisfy a given criterion. Several such methods have been proposed for the segmentation of SAR images. The criteria used for merging neighbouring regions are mostly based on the statistical distribution of the values inside each of the regions:

- Lombardo [51] uses a maximum likelihood ratio based on a gamma-distribution for segmenting multi-look intensity images

- Fjörtoft [52] combines an edge detector with a watershed algorithm to obtain an over-segmented image and then merges adjacent regions based on a likelihood ratio criterion

- Cook and Mc Connell [53] define the criterion for merging on the basis of an uni-variate hypothesis test (the Student test). In [54] the method is improved using a likelihood ratio test in stead of the Student test and combining it with simulated annealing.

Several authors (e.g. [25, 30, 54]) have suggested to use a Markov Random Field model (MRF) for segmentation of SAR images.

In the previous chapter we have seen that multi-variate hypothesis test offer a powerful way to adapt methods suited for mono-polarisation SAR images to polarimetric images. Hence the idea to adapt the method of Cook, called *Merge Using Moments (MUM)* [53] to the problem at hand. MUM is a pure merge method, i.e. it starts from small areas of the image which are supposed to be homogeneous and then merges neighbouring areas if they comply with some similarity measure. The method thus starts from an initial over-segmentation of the image. This initialisation divides the images in small squares. The choice of the size of these initial squares is very important. The final segmentation will not discern anything smaller than this initial segmentation so starting regions should not be taken to large. On the other hand if the initial regions are too small the presence of speckle will make the statistical comparison between neighbouring regions unreliable. In fact when the initial regions are too small the segmentation will follow local structures in the speckle which results in very irregularly shaped small regions. In the single-look images we used; an initial size of at least 7×7 pixels is necessary.

In the original method [53] a Student-t test is used to compare adjacent regions. The results of this method are discussed in the next section. Then the results of the extension of the Student-t test to multi-variate data, i.e. the Hotellings T^2 are discussed.

In section 6.1.3 a method based on the Mahalanobis distance is proposed. The Student-t test and the method using the Mahalanobis distance are adapted to uni-modal symmetrical distributions. If the number of samples of both populations to be compared is unequal, the Hotellings test also requires uni-modal symmetrical distributions. Therefore we will apply the three variations of MUM on the log-intensity image in which the speckle in uniform regions has a more symmetrical distribution (a Fisher-Tippet distribution).

6.1.1   MUM based on Student-T Test

In the paper in which Cook et al.[53] introduce the MUM method, the Student-t test for significantly different means is used as a merge criterion. Given two regions A and B containing resp. N_A and N_B pixels, the average and variance in both regions , (μ_A, σ_A^2) and (μ_B, σ_B^2), are estimated. Then the pooled variance is calculated:

$$\sigma_{A,B}^2 = \frac{N_A \sigma_A^2 + N_B \sigma_B^2}{N_A + N_B - 2}, \tag{6.1}$$

and the standard error of the difference of means is:

$$\sigma_D^2 = \sigma_{A,B}^2 \left(\frac{1}{N_A} + \frac{1}{N_B} \right). \tag{6.2}$$

Please note that this is again based on the assumption of independent observations within each sample. The t-test statistic is then defined as:

$$t = \frac{|\mu_A - \mu_B|}{\sigma_D}. \tag{6.3}$$

This follows a Student's T distribution with $\nu = N_A + N_B - 2$ degrees of freedom. If the regions contain enough (> 30) pixels the Student's T distribution can be approximated by a $\mathcal{N}(0,1)$ distribution. The threshold can thus, in principle, be determined theoretically. However, Cook et al. [53] say that "in practice a value of 10^{-4} is found to give an acceptable segmentation for many kinds of images". In the image we tried to segment, a threshold of 10^{-4} was also found to give good results. This low thresholds can partly be explained by the spatial correlation in the images and by the fact that the student test becomes too strict as the number of samples increases.

The results of MUM using a Student's T-test and applying a threshold of 10^{-4} is given in fig. 6.1, for each polarisation separately. As a reference the original image (HH log-intensity image) is also shown and some large objects were delimited manually.
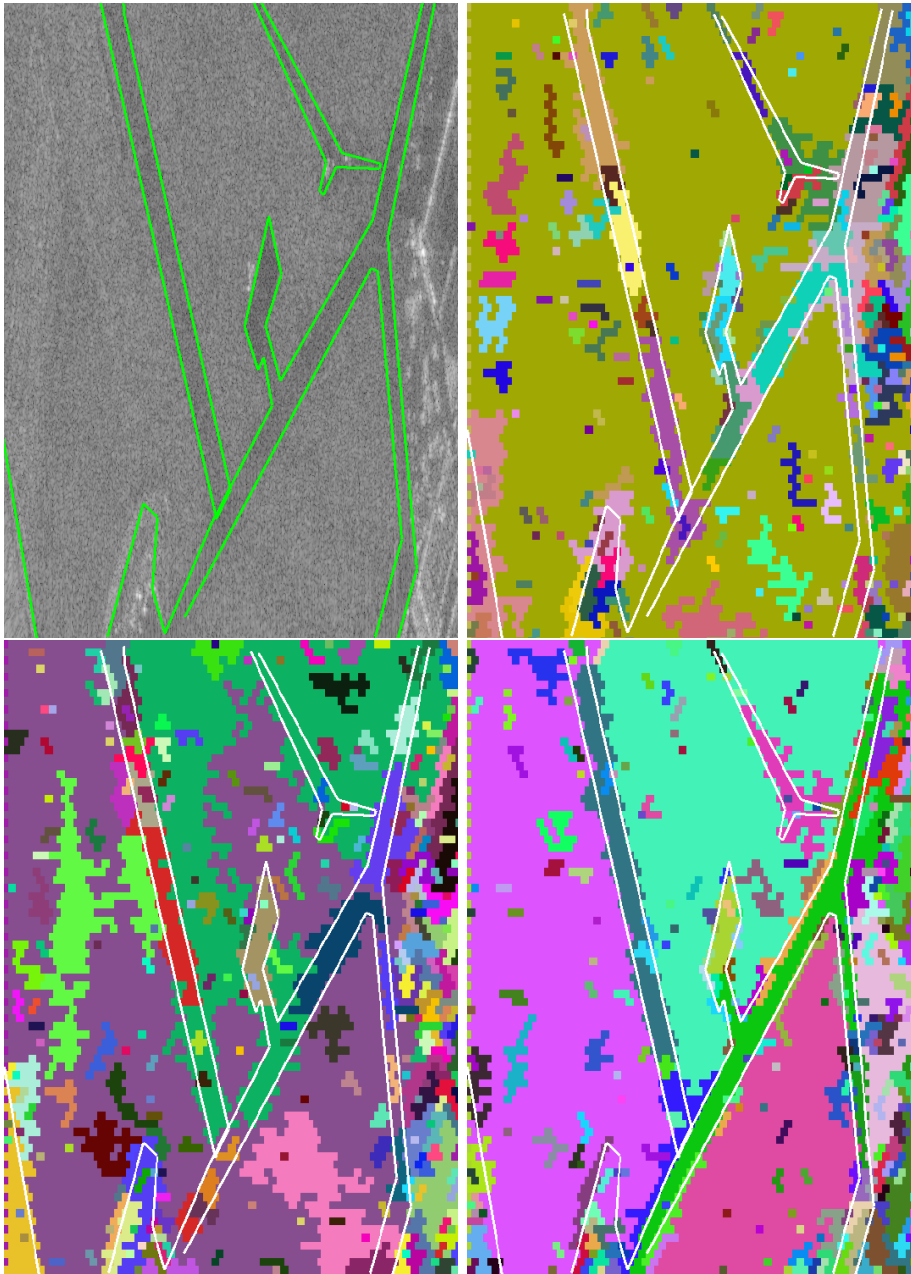
Figure 6.1: Original image and results of MUM segmentation based on Student's test for HH(upper right), HV(lower left) and VV(lower right)

The results of fig. 6.1 were obtained by applying the MUM segmentation with the same threshold on the log-intensity images of the three polarisation. The best results are obtained for the VV polarisation. For the HH-component some parts of the taxiway in the central lower part of the image have already been merged with the surrounding grass while the uniform regions between the taxiways have not yet been fully merged. The same is true for the results of the HV-component image where even larger parts of the uniform

regions have not been merged while much of the taxiway has been lost. The parts that were not correctly segmented are not the same in the three images. Hence the idea of applying the segmentation to the three polarisations at the same time. As already seen in the previous chapter, multi-variate methods can be used to achieve such a segmentation. Two multi-variate segmentation methods, applying the MUM-principle to the complete polarimetric image at once are presented in the next two sections.

6.1.2 MUM based on Hotellings T^2 Test

The evident extension of the original MUM algorithm to multi-variate data consists in replacing the Student's T test by a Hotellings T^2 test (see also 5.4.2). The Hotellings T^2 test is a multi-variate hypothesis test for the difference of means. The test statistic for the Hotellings test is defined in 5.4.2. It takes into account the average (pooled) polarimetric covariance matrix of the two regions for which the difference of means is tested. By applying a threshold on the test statistic a segmentation method can be built. The results of a segmentation based on this method using a threshold of 10^{-9} is given in fig. 6.2.

Figure 6.2: Results of MUM segmentation based on Hotellings test

6.1.3 MUM based on Mahalanobis Distance

This method is based on the calculation of the Mahalanobis distance between the average vector of one region and the other region. The Mahalanobis distance is defined as:

$$D_{Mahal} = (\overline{\mathbf{X_1}} - \overline{\mathbf{X_2}})^t \mathbf{C_1}^{-1} (\overline{\mathbf{X_1}} - \overline{\mathbf{X_2}}). \tag{6.4}$$

This is similar to the definition of the T^2 statistic (in eq. 5.18). The differences are the scaling factor and the fact that the covariance matrix of one region is used in stead of the pooled covariance matrix of both regions.

The largest region is used to calculate the covariance matrix. The purpose of the test that we would like to develop is to decide whether a given smaller region has an average that is close enough to the average of the larger region for the two regions to be merged.

If a uniform region is characterised by a multi-variate normal distribution, the square of the Mahalanobis distance of its elements follows a χ^2 distribution with degree of freedom equal to the number of variables [36]. However, when calculating the average of a region, the Mahalanobis distance of this average will be much smaller than that of the individual pixels in the region because we approach the average of the underlying distribution.

Moreover, due to the spatial correlation in the SAR images, the elements of the covariance matrix will be underestimated. Furthermore, the quality of the estimate of both the covariance matrix and the mean vectors is influenced by the number of pixels that are used for the estimation. The combination of these effects leads to an underestimation of the Mahalanobis distance.

This means that a CFAR threshold will be a function of:

- The spatial correlation of the SAR sensor

- The number of pixels used to estimate the covariance matrix (size of region 1): N_{ref}

- The number of pixels used to calculate the mean (size of region 2): N_{mean}

In order to find this threshold we simulated Fisher-Tippet (eq. 4.9) distributed data (corresponding to log-intensity data) with a spatial correlation corresponding to the one found for the sensor (see chapter 4). For one combination of N_{ref} and N_{mean} a large number of samples was drawn and the histogram of the Mahalanobis distance calculated. From this histogram the $5, 1, 0.5$ and 0.1% false alarm thresholds were determined. Varying both N_{ref} and N_{mean} a 3D surface of thresholds is obtained (see fig. 6.3).
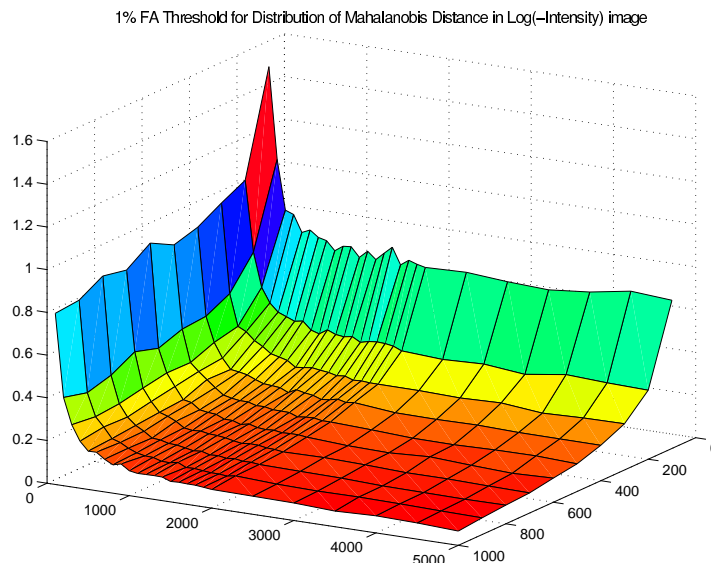

Figure 6.3: 1% false alarm threshold for Mahalanobis distance vs. N_{ref} and N_{mean}

This surface is used to adapt the threshold during the merge process, i.e. the threshold decreases as the size of the compared regions increases. Please note that, for the influence of the spatial correlation, this method is only an approximation because the regions are considered to be squares. As the spatial correlation is different in range and in azimuth, the threshold should depend on the form of each region. Taking this into account would make the algorithm very heavy.

The order in which the regions are merged in each step is very important. Some tests have shown that the best results are obtained when at each iteration the regions, for which the ratio between the Mahalanobis distance and the found threshold is smallest, are merged first. This means that, for the same Mahalanobis distance, small regions are merged first.

The results of a segmentation based on this method using the 0.5% threshold is given in fig. 6.4.
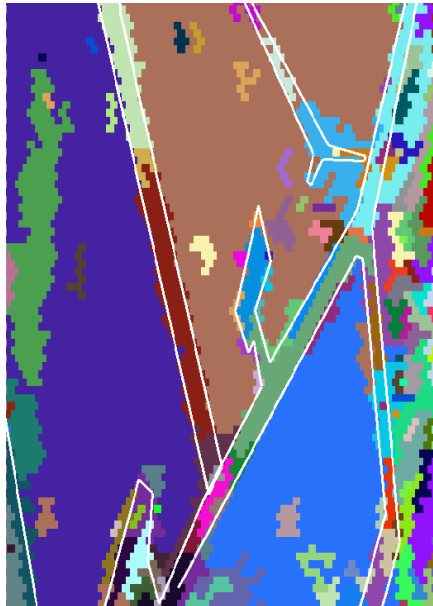

Figure 6.4: Results of MUM segmentation based on Mahalanobis distance

The method based on the Mahalanobis distance seems to give the best results. Some "false regions" are found when the initial segmentation overlaps to regions in the image. Examples of this problem can be seen next to the taxiways.

6.2   Image Classification using Decomposition Algorithms

The differences between the various polarisations are due to the scattering mechanisms in the different objects in the scene. If the polarimetric data can be decomposed into contributions of different scattering mechanisms it is therefore possible to develop an image classification method that is based on the physical characteristics of the objects in the scene. These decomposition algorithms can be well adapted to detect large uniform regions corresponding to main classes of scattering. As we are, in a first phase, not interested in detecting different types of fields but only in finding cities, forests and fields, using a classification based on these decomposition methods can be useful. Many decomposition techniques have been proposed in the literature [19, 55, 56, 57, 58]. In [20] an overview is given. The different decomposition methods are subdivided in three categories:

- methods based on the Müller matrix

- methods based on an eigenvalue/eigenvector analysis of the covariance matrix (eq. 3.38) or the coherency matrix (eq. 3.39)

- methods using a coherent decomposition of the scattering matrix

We have particularly focused on the methods that decompose the polarimetric data in basic physical scattering mechanisms that can be linked to different types of terrain (landcovers).

The decomposition methods are applied directly on the polarimetric image, calculating the necessary parameters in sufficiently large rectangles. However, choosing these rectangles a priori, can lead to mixtures of scattering mechanisms within one rectangle. For some applications it could be better to first segment the image using for instance the methods described in the previous section and to calculate the average scattering mechanism in each of these regions.

The first two decomposition methods that are explored below (i.e. Van Zyl's [55] and Freeman's [56] decomposition) assume reflection symmetry which results in a decorrelation between co-polarised and cross-polarised channels [59]. Although this is a valid assumption in most low vegetated areas, it is not true in areas corresponding to e.g. cities or forests as can be verified by looking at the inter-channel correlation for different types of land-cover presented in section 4.2.3. A decomposition method that does not rely on the assumption of reflection symmetry is the method proposed by Cloude and Pottier [57] and its extension by Pottier and Lee [58].

6.2.1   Van Zyl's Decomposition

Van Zyl [55] (see also [25]) proposes a method to decompose the backscattering in contributions of three scattering mechanisms:

- Scattering involving an odd number of reflections

- Scattering involving an even number of reflections

- Diffuse scattering

According to Van Zyl, in the case of a single reflection, HH and VV are in phase, thereafter, each new reflection adds a phase difference of $180°$. For a diffuse scattering HH and VV are uncorrelated and the phase difference is uniformly distributed. Under the hypotheses that HV=VH and that co- and contra-polarisations are uncorrelated these three conditions can be expressed as:

1. $arg(S_{HH}S_{VV}^*) \approx 0° \Rightarrow \langle Re(S_{HH}S_{VV}^*) \rangle > 0$

2. $arg(S_{HH}S_{VV}^*) \approx 180° \Rightarrow \langle Re(S_{HH}S_{VV}^*) \rangle < 0$

3. $arg(S_{HH}S_{VV}^*) \approx any \Rightarrow \langle Re(S_{HH}S_{VV}^*) \rangle \approx 0$

Van Zyl's algorithm can thus be summarized by:

Algorithm 1

if $| \langle Re(S_{HH}S_{VV}^*) \rangle | < \langle | S_{HV} |^2 \rangle \Rightarrow$ Diffuse scattering.
else
. if $\langle Re(S_{HH}S_{VV}^*) \rangle > 0 \Rightarrow$ Odd number of reflections
. if $\langle Re(S_{HH}S_{VV}^*) \rangle < 0 \Rightarrow$ Even number of reflections

Note that comparing the value of $| \langle Re(S_{HH}S_{VV}^*) \rangle |$ to $| \langle S_{HV} \rangle |$ instead of comparing to 0 allows to cope with the large variations of the phase that are usually encountered and caused by speckle. The hypotheses made in this methods are:

1. reciprocity: $S_{HV} = S_{VH}$.

2. Reflection symmetry. This causes the co- and contra polar channels to be decorrelated.

3. Predominance of the co-polar on the cross-polar channels, i.e. $S_{HV} << S_{HH}$ and $S_{HV} << S_{VV}$.

4. Limited noise

The first hypothesis is automatically verified in the a mono-static geometry (backscattering). The second hypothesis is not automatically satisfied. If it is not satisfied Van Zyl [55] labels the pixel as unclassified while Mascle [25] detects this problem and assigns the new class: "anisotropic scatterers" to it. The lack of reflection symmetry can be checked by calculating the cross-channel correlation coefficient [25]:

$$\rho_{hhhv} = \frac{| \langle S_{HH}S_{HV}^* \rangle |}{\sqrt{\langle | S_{HH} |^2 \rangle \langle | S_{HV} |^2 \rangle}}. \tag{6.5}$$

If this value is above a given threshold, the pixel is said to belong to the class of anisotropic targets. Le Hégarat-Mascle [25] set this threshold by calculating ρ_{hhhv} on the complete image and determining the mean μ_{hhhv} and standard deviation σ_{hhhv} for the complete image. The threshold is then empirically set to $\mu_{hhhv} + 1.5\sigma_{hhhv}$. The third hypothesis can be verified and when the cross-polar component is larger than the co-polar ones, the

pixel is labeled as unclassified. The last hypothesis will be verified if the windows in which the averages are calculated are large enough.
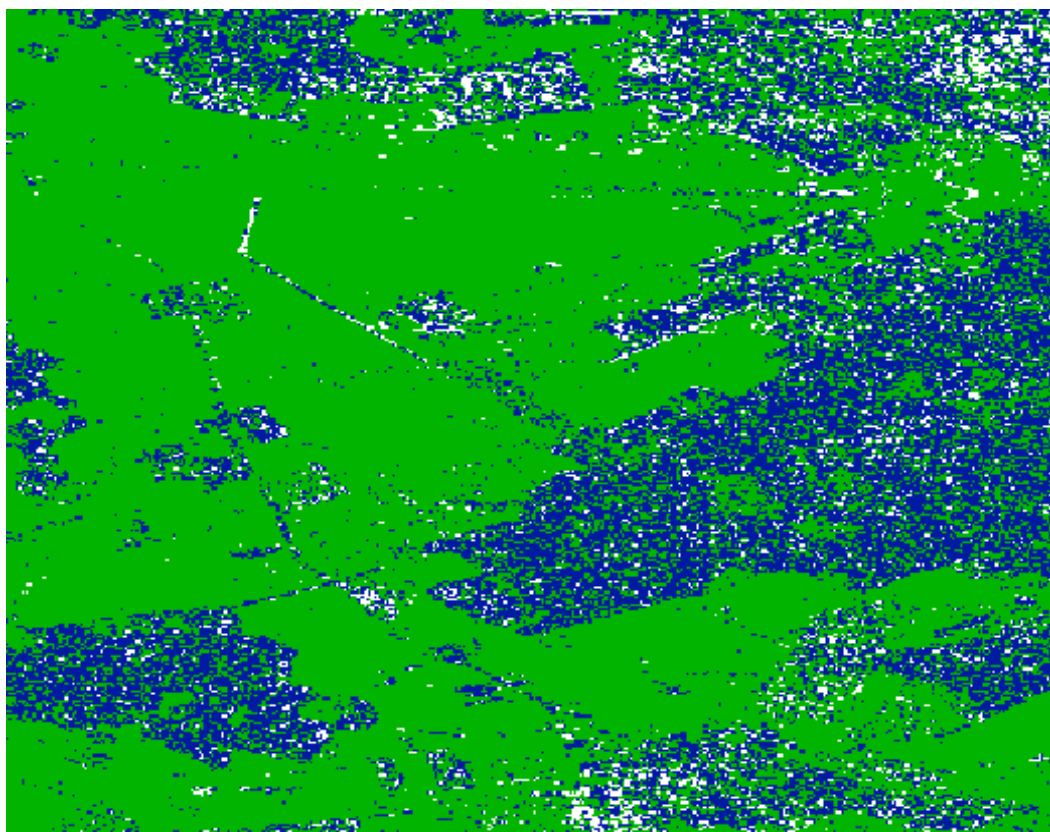
🟩 Odd number of reflections (Surface scattering)   🟦 Diffuse (volume) scattering

⬜ Even number of reflections (Double bounce)

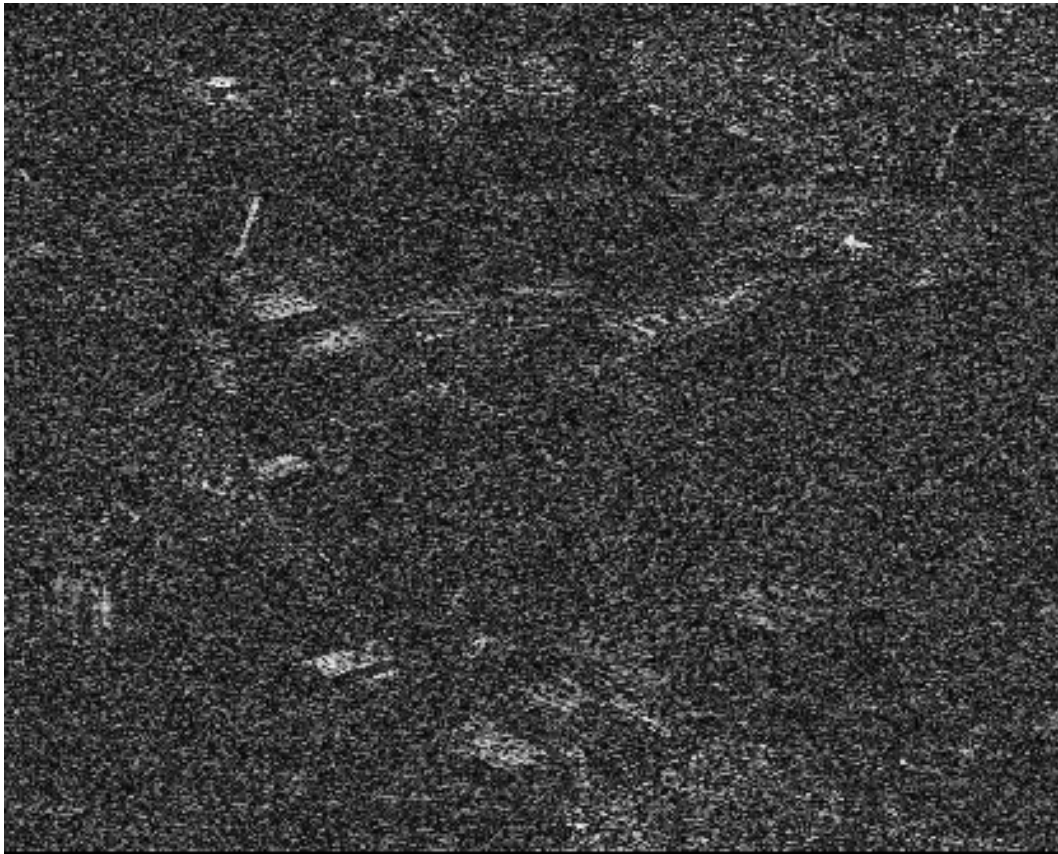Figure 6.5: Classification using Van Zyl's algorithm

Figure 6.6: Image of ρ_{hhhv}

In fig. 6.5 the results of the classification are shown. Fig. 6.6 shows the correlation coefficient rescaled between 0(black) and 1.0 (white). It can be seen that in most fields as well as on large roads the main class is "Odd number of reflections". For the largest part forests and villages appear as "diffuse scatterers" while some buildings as well as some individual pixels in forests (trees) are classed as "Even number of reflections". High values of ρ_{hhhv} are seen in some buildings as well as some fields. These fields can show an asymmetry due to recent ploughing or harvesting (when plants are left in the field and present a preferential orientation).

6.2.2 Freeman's Decomposition

In [56] a method is proposed to decompose the polarimetric covariance matrix in contributions of three scattering mechanisms:

- Volume scattering

- Surface scattering (by a slightly rough surface)

- Double Bounce

The volume scattering is modeled as the scattering by a cloud of randomly oriented cylinder-like scatterers. One scatterer in standard orientation has the following scattering matrix:

$$S = \begin{bmatrix} S_{hh} & S_{hv} \\ S_{vh} & S_{vv} \end{bmatrix} = \begin{bmatrix} a & 0 \\ 0 & d \end{bmatrix}. \tag{6.6}$$

If the orientation of scatterers is randomly distributed around the radar look direction, the radar return for one scatterer is found by rotating first into a coordinate system with vertical along the scatterer's standard orientation, calculating the scattered field and rotating back.

$$S = \begin{bmatrix} S_{hh} & S_{hv} \\ S_{vh} & S_{vv} \end{bmatrix} \begin{bmatrix} a cos^2\Phi + d sin^2\Phi & (d-a)cos\phi sin\Phi \\ (a-d)cos\phi sin\Phi & a sin^2\Phi + d cos^2\Phi \end{bmatrix}. \tag{6.7}$$

If $p(\Phi)$ is the probability density function for the orientation of the scatterers, the expected values for any function of Φ is defined as:

$$< f >_e = \int_0^{2\pi} f(\Phi)p(\Phi)d\Phi, \tag{6.8}$$

in which $< \, . \, >_e$ denotes an ensemble average. From this the elements of the average covariance matrix can be found. Freeman uses his volume scattering to model the scattering by forest canopy, he therefore assumes very thin cylinders (dipoles) In this case $a = 0$ and $d = 1$. If the orientation of the scatterers is uniformly distributed, after normalisation (i.e. setting $<| S_{vv} |^2> = 1$), this results in:

$$\begin{array}{llll} \langle | S_{hh} |^2 \rangle & = \langle | S_{vv} |^2 \rangle & = 1 \\ \langle S_{hh}S_{vv}^* \rangle & = \langle | S_{hv} |^2 \rangle & = 1/3 \\ \langle S_{hh}S_{hv}^* \rangle & = \langle S_{hv}S_{vv}^* \rangle & = 0 \end{array} \tag{6.9}$$

The double bounce scattering component is modeled by the scattering from a dihedral corner reflector. The two reflector surfaces can be made of different dielectric materials. As Freeman initially introduced his decomposition method to model scattering in vegetated areas, the double bounce is mainly meant to be between the soil and tree trunks, and therefore he introduces a phase term to incorporate the effect of attenuation and phase change due to the propagation through the canopy layer. This results in:

$$S = \begin{bmatrix} S_{hh} & S_{hv} \\ S_{vh} & S_{vv} \end{bmatrix} = \begin{bmatrix} e^{j2\gamma_h}R_{gh}R_{th} & 0 \\ 0 & e^{j2\gamma_v}R_{gv}R_{tv} \end{bmatrix}, \tag{6.10}$$

in which γ is the complex propagation factor and R_t and R_g are the Fresnel coefficients for respectively the tree trunk and the ground. This results in:

$$\begin{array}{ll} \langle | S_{hh} |^2 \rangle & = | \alpha |^2 \\ \langle | S_{vv} |^2 \rangle & = 1 \\ \langle S_{hh}S_{vv}^* \rangle & = \alpha \\ \langle | S_{hv} |^2 \rangle & = \langle S_{hh}S_{hv}^* \rangle = \langle S_{hv}S_{vv}^* \rangle = 0, \end{array} \tag{6.11}$$

in which $\alpha = e^{j2(\gamma_h - \gamma_v)}\frac{R_{gh}R_{th}}{R_{gv}R_{tv}}$ is thus complex.

For the surface scattering a first-order Bragg model is used. This gives:

$$\begin{aligned}
\langle\, |\, S_{hh}\, |^2\, \rangle &= |\, \beta\, |^2 \\
\langle\, |\, S_{vv}\, |^2\, \rangle &= 1 \\
\langle S_{hh} S_{vv}^* \rangle &= \beta \\
\langle\, |\, S_{hv}\, |^2\, \rangle &= \langle S_{hh} S_{hv}^* \rangle = \langle S_{hv} S_{vv}^* \rangle = 0,
\end{aligned} \tag{6.12}$$

in which β is real.

The elements of the covariance matrix are now written as a sum of the contributions of the three scattering mechanisms:

$$\begin{aligned}
\langle\, |\, S_{hh}\, |^2\, \rangle &= f_s\, |\, \beta\, |^2 + f_d\, |\, \alpha\, |^2 + f_v \\
\langle\, |\, S_{vv}\, |^2\, \rangle &= f_s + f_d + f_v \\
\langle S_{hh} S_{vv}^* \rangle &= f_s \beta + f_d \alpha + f_v/3 \\
\langle\, |\, S_{hv}\, |^2\, \rangle &= f_v/3 \\
\langle S_{hh} S_{hv}^* \rangle &= \langle S_{hv} S_{vv}^* \rangle = 0
\end{aligned} \tag{6.13}$$

where f_s, f_d and f_v are the surface, double-bounce and volume (or canopy) contributions to the VV cross section. Since neither the surface nor the double bounce scattering contribute to the HV term, we can estimate the volume scattering directly and subtract the term from the other equations yielding:

$$\begin{aligned}
A_{hh} &= \langle\, |\, S_{hh}\, |^2\, \rangle - f_v = & f_s\, |\, \beta\, |^2 + f_d\, |\, \alpha\, |^2 \\
B_{vv} &= \langle\, |\, S_{vv}\, |^2\, \rangle - f_v = & f_s + f_d \\
C_{hhvv} &= \langle S_{hh} S_{vv}^* \rangle - f_v/3 = & f_s \beta + f_d \alpha
\end{aligned} \tag{6.14}$$

Then, as in Van Zyl [55], it is decided whether double-bounce or surface scatter is the dominant contribution in the residual, based on the sign of the real part of $S_{hh}S_{vv}^*$:

$$if \quad Re(S_{hh}S_{vv}^*) \quad \begin{aligned} &> 0 \quad \alpha = -1 \\ &< 0 \quad \beta = 1. \end{aligned} \tag{6.15}$$

These assumptions allow to determine the remainder of the parameters: f_s, f_d and α or β:

If $\alpha = -1$, i.e. when surface scattering is dominant we get:

$$\begin{aligned}
f_s &= \frac{|<C_{hhvv}>|^2 + B_{vv}^2 + 2B_{vv}Re(<C_{hhvv}>)}{A_{hh} + B_{vv} + 2Re(C_{hhvv})} \\
f_d &= B_{vv} - f_s \\
\beta &= \frac{Re(C_{hhvv}) + f_d}{f_s}
\end{aligned} \tag{6.16}$$

In the other case, i.e. when the double-bounce is dominant ($\beta = 1$).

$$\begin{aligned}
f_d &= \frac{|<C_{hhvv}>|^2 + B_{vv}^2 - 2B_{vv}Re(<C_{hhvv}>)}{A_{hh} + B_{vv} - 2Re(C_{hhvv})} \\
f_s &= B_{vv} - f_d \\
Re(\alpha) &= \frac{Re(C_{hhvv}) - f_s}{f_d} \\
Im(\alpha) &= \frac{Im(C_{hhvv})}{f_d}
\end{aligned} \tag{6.17}$$

Finally they estimate the contribution of each scattering mechanism to the total received power:

$$P = P_s + P_d + P_v = (\mid S_{hh} \mid^2 + 2 \mid S_{hv} \mid^2 + \mid S_{vv} \mid^2), \qquad (6.18)$$

with

$$\begin{aligned} P_s &= f_s(1 + \mid \beta \mid^2), \\ P_d &= f_d(1 + \mid \alpha \mid^2), \\ P_v &= 8f_v/3. \end{aligned} \qquad (6.19)$$

We have performed this decomposition on the L-band images of Oberpfaffenhofen. The ensemble averages were taken on a 10 by 4 pixel area (10 in azimuth, 4 in range). For visual inspection of the results, in fig. 6.7 a color composite image is shown in which the red component represents Pd, the green Ps and the blue Pv. In most of the fields the predominant scattering component is Ps (surface scattering). Some isolated buildings have either a high Pd or a combination of Ps and Pd. In villages and forests the three components are represented. However, in forests there is no correlation between adjacent pixels while in villages small rectangular structures (mainly combinations of Pd and Ps, thus red, yellow or orange) appear. One of the roads has the appearance of a long line of "forest". This is caused by trees lining the roads. The runway and main taxiways of the airfield appear as very dark green. This indicates a very low backscattering mainly due to surface scattering. This decomposition seems very interesting. It provides a way to associate a simple physical meaning to the polarimetric measurements and should allow for a first automatic classification.
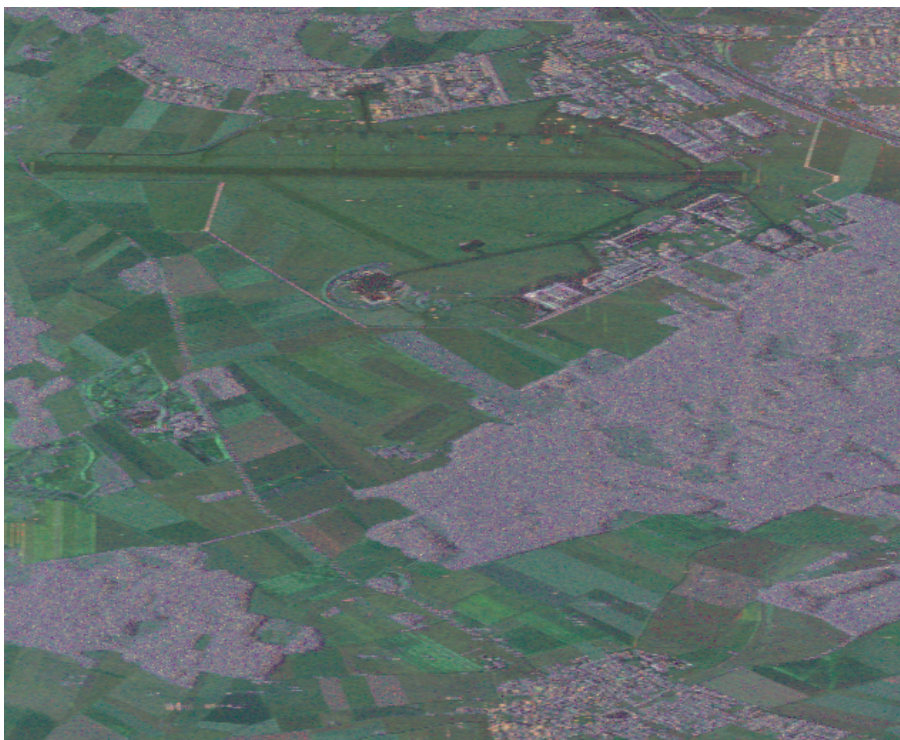

Figure 6.7: Composite image of elementary scattering contributions (red: double bounce, green: surface, blue: volume)

From this image it is clear that fields at one hand and forests and built-up areas on the other hand can be directly distinguished based on the relative contribution of each of the three scattering mechanisms. Hence the idea to order the contribution of each scattering mechanism in each pixel of the image and to assign a class to each of the possible orderings (permutations). For three scattering mechanisms we thus get 6 classes. Because of the presence of speckle, the ordering for uniform regions does not appear to be completely uniform (although in the Freeman algorithm we already averaged over 10×4 pixels). In each pixel we therefore assign the class that is most prominent (majority voting), again over a neighbourhood, i.e. a square window around the current pixel. The agreement of pixels in the neighbourhood can then be used as a measure of the confidence in the classification. This idea has not yet been exploited. The results of this simple classification are shown in fig. 6.8. The definition of the 6 classes is shown in the figure as well.

LEGEND:

■ Class 1: Pd >= Ps >= Pv

■ Class 2: Pd >= Pv >= Ps

■ Class 3: Ps >= Pd >= Pv

□ Class 4: Ps >= Pv >= Pd

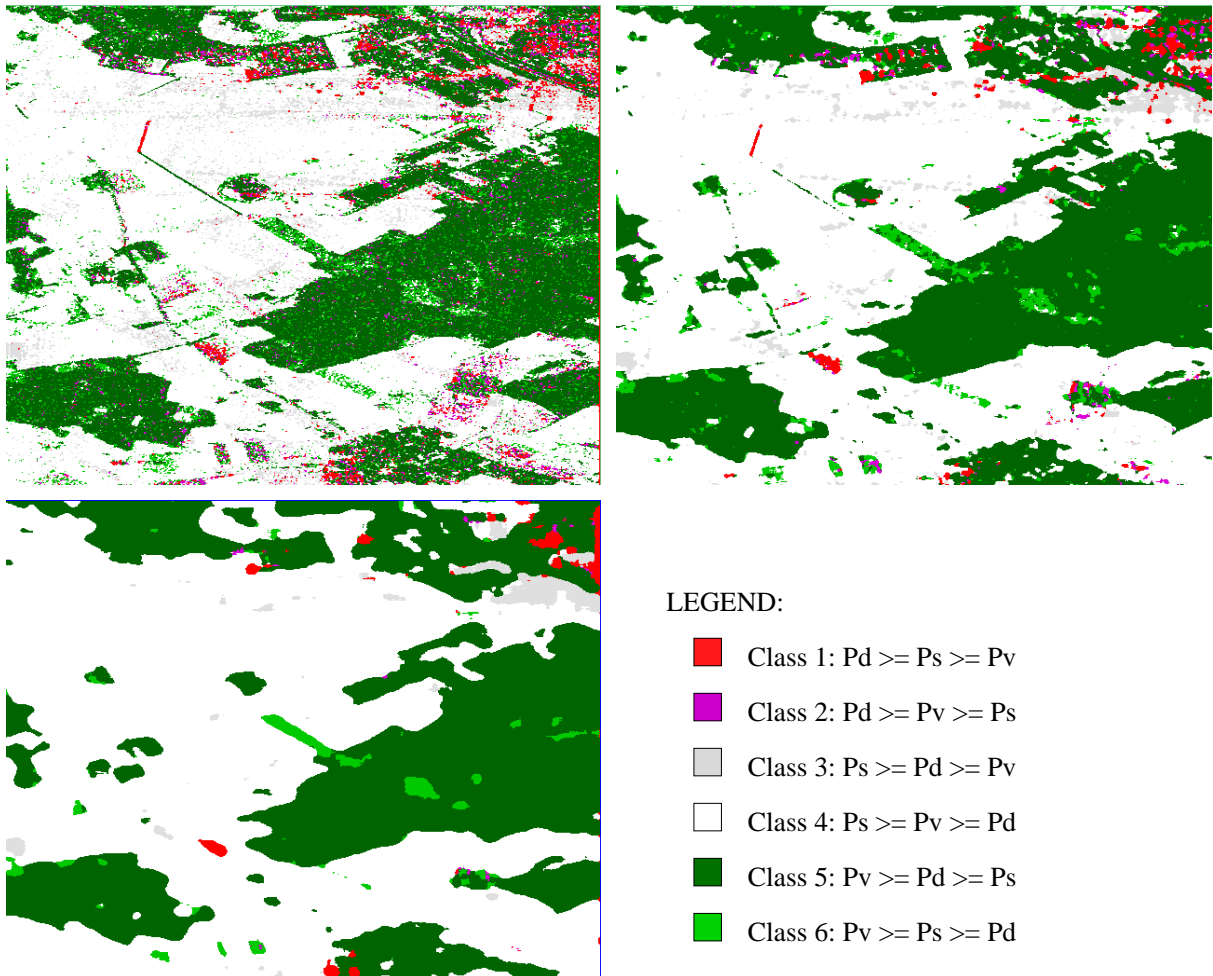■ Class 5: Pv >= Pd >= Ps

■ Class 6: Pv >= Ps >= Pd

Figure 6.8: Results of classification based on single pixels (a), majority voting in a 4x4 window (b) and majority voting in a 10x10 window (c)

The classes where volume scattering is predominant (the yellow and dark green areas in the figures) mainly correspond to forests and parts of built-up areas. The Freeman decomposition as it is applied here thus allows to distinguish the regions corresponding either forests or built-up areas from the remainder of the image.

6.2.3 Cloude's Decomposition

The decomposition method introduced by Cloude and Pottier [57] is based on an eigenvalue/eigenvector analysis of the polarimetric coherency matrix $[T]$ (see eq. 3.39). The coherency matrix can be diagonalised as follows:

$$< [T] >= [U_3] \begin{bmatrix} \lambda_1 & 0 & 0 \\ 0 & \lambda_2 & 0 \\ 0 & 0 & \lambda_3 \end{bmatrix} [U_3]^+ . \tag{6.20}$$

The $^+$ denotes the complex conjugate, transpose matrix, i.e. the adjoint matrix. The λ_i's are the real eigenvalues and U_3 is a unitary matrix whose columns are the orthonormal eigenvectors of $[T]$. The eigenvalues are ordered such that $\lambda_1 \geq \lambda_2 \geq \lambda_3$.

The eigenvectors correspond to different scattering mechanisms occurring in the area over which the coherency matrix is averaged [57]. The eigenvalues give the weight of each of the three scattering mechanisms. If only one eigenvalue differs from zero, there is only one scattering mechanism. Hence the idea of introducing, what turned out to be an important physical parameter, the scattering entropy H which gives a global measure of the distribution of the scattering process and is defined as:

$$H = \sum_{i=1}^{3} P_i log_3(P_i) \quad with: \quad P_i = \frac{\lambda_i}{\sum_{i=1}^{3} \lambda_i} . \tag{6.21}$$

If H is very low there is one dominant scattering mechanism and the system can be represented by one single scattering matrix. As H increases, the target is depolarising and it can no longer be considered as having a single scattering matrix. The scattering is a combination of different scattering mechanisms. In the limit where H=1 the polarisation information becomes zero and the target scattering becomes a random noise process; the radar response is then completely depolarised.

The eigenvectors $\underline{e_i}$ can be parametrised as follows [57]:

$$\underline{e_i} = \begin{bmatrix} cos\alpha_i & sin\alpha_i cos\beta_i e^{i\delta} & sin\alpha_i sin\beta_i e^{i\gamma} \end{bmatrix}^T . \tag{6.22}$$

The α angle determines the type of scattering mechanism, ranging from 0° for isotropic surface scattering through 45° for linear dipole scattering, over double bounce scattering between two dielectric surfaces, to 90° for dihedral scattering from metal surfaces. In fig. 6.9 a schematic representation of the physical interpretation of α is shown.
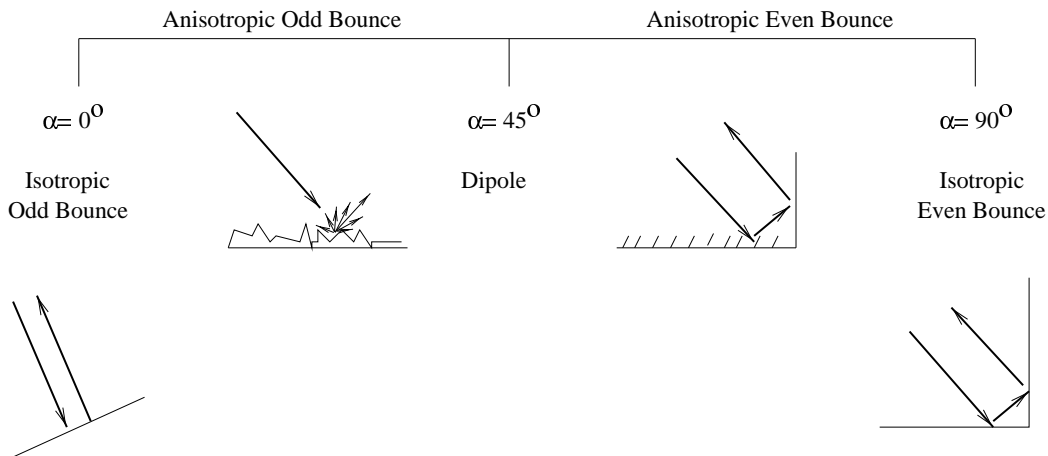
Anisotropic Odd Bounce   Anisotropic Even Bounce

$\alpha= 0^O$ $\alpha= 45^O$ $\alpha= 90^O$

Isotropic   Dipole   Isotropic
Odd Bounce   Even Bounce

Figure 6.9: Interpretation of the α angle (reproduced from [60])

The β angle represents the orientation of the target and can vary between 0 and 180°. δ and γ are phase angles. For the 5 parameters of the eigenvectors the mean values for the dominant scattering are determined as a weighted sum with weights P_i, e.g. for α:

$$\overline{\alpha} = \sum_{i=1}^{3} P_i \alpha_i. \tag{6.23}$$

In [57] a classification method is proposed on the basis of the entropy H and this averaged α. The H, α space is divided into 8 regions of basic scattering behaviour. The boundaries of the regions given in the article were chosen "generically", based on the general scattering mechanisms. The entropy is divided in low ($H \leq 0.5$), medium ($0.5 < H < 0.9$) and high ($H \geq 0.9$). The boundaries for α depend on the entropy region and are given below. The 8 regions according to [57] are enumerated below:

- **Zone 8: Low Entropy Surface scattering ($\alpha < 42.5^o$):** water, ice and very smooth land surfaces fall into this category. In fact all odd-bounce scattering falls here (including scattering from triheders).

- **Zone 7: Low Entropy Dipole scattering ($42.5^o < \alpha < 47.5^o$):** in this region mechanisms with a large imbalance between the amplitude of HH and VV will fall. Examples are vegetation with strongly correlated orientation of anisotropic scattering elements

- **Zone 6: Low Entropy "Multiple" scattering ($\alpha > 47.5^o$):** what is meant here is even-bounce scattering, in particular scattering from isolated dielectric or metallic diheders

- **Zone 5: Medium Entropy Surface scattering ($\alpha < 40^o$):** The increased entropy can be due to an increase in surface roughness or to canopy propagation effects. This region will thus contain sparse or low vegetation.

- **Zone 4: Medium Entropy Vegetation scattering** ($40^o < \alpha < 50^o$): The increased entropy is due to a statistical distribution of the orientation angle of the scatterers.

- **Zone 3: Medium Entropy Multiple scattering** ($\alpha > 50^o$): This corresponds to dihedral scattering with moderate entropy and can occur for example in forests where, in L- or P-band double bounce scattering may occur after propagation through forest canopy.

- **Zone 2: High Entropy Vegetation scattering** ($45 < \alpha < 55^o$): An example is single scattering from a cloud of needle-like particles. This is mainly scattering by leafs and small branches of trees.

- **Zone 1: High Entropy Multiple scattering** ($\alpha > 55^o$): This corresponds to double-bounce scattering in forests with a well-developed crown.

In the article [57] 9 regions were mentioned. The region corresponding to high entropy surface scattering ($\alpha < 45^0$) is however a region that is not feasible, i.e. it is not possible to distinguish surface scattering with an entropy $H > 0.9$. In fig. 6.10 the Cloude classification with the boundaries mentioned above is applied on a L-Band SAR image.
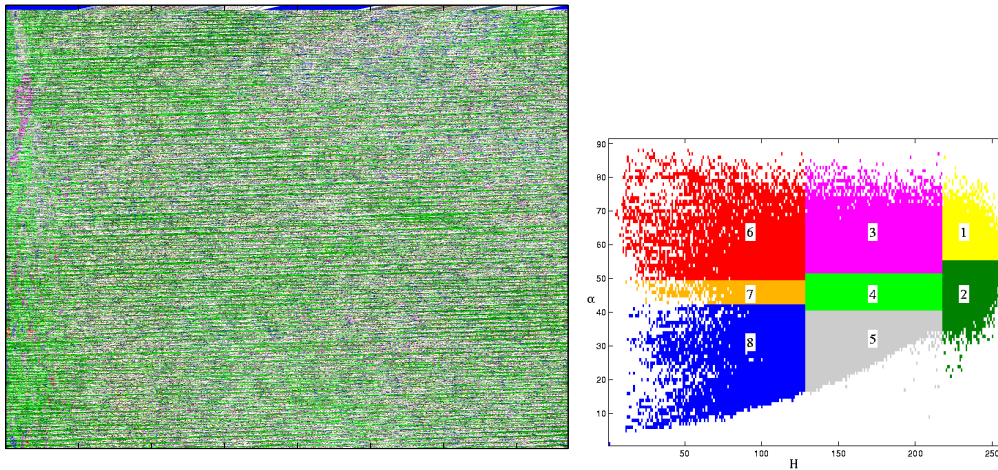

Figure 6.10: Result of Cloude decomposition into 8 classes and the corresponding H/α plot (H was multiplied with 255)

Several remarks are in order. First of all, the number of different scattering types in the model is perhaps too high for our purposes. Remember that we wish to distinguish forests from low vegetation and built-up areas, and perhaps main roads or other very smooth surfaces. Another point is that the boundaries delimiting the 8 regions above were chosen somewhat arbitrarily. The actual boundaries depend on radar calibration, measurement noise floor, the variance of parameter estimates, etc. Because the boundaries are not clearly defined, fuzzyfying them could be a solution. Hellmann [60] proposes, among other methods, a rule-based fuzzy system for classification in the H/α space. Here the entropy

and α are both subdivided according to fuzzy membership functions (e.g. low, medium, high) and to lancover type of interest some rules are assigned.

The fuzzy classification gives a membership in each pixel of the image for each type of landcover that was defined. A majority rule is then applied to give the final classification result. In annex D details of the fuzzy rule-based system are given.

The result of such a classification of the H/α space is presented in fig. 6.11(left).

The entropy is a measure for the fact whether one or more scattering mechanisms are occurring in the "resolution cell" of the algorithm. If the entropy is larger than zero, more than one eigenvalue of the coherency matrix is different from zero. However the entropy does not give any information about the presence of 2 or 3 non-zero eigenvalues or the relative importance of the two non-dominant eigenvalues. The anisotropy A, introduced by Pottier [61, 58] copes with this problem. It is defined as:

$$A = \frac{\lambda_2 - \lambda_3}{\lambda_2 + \lambda_3}. \tag{6.24}$$

A low value for the anisotropy means the second and third scattering mechanisms are equivalent. If A is high, the second is larger than the third. If the entropy is very low, there is only one important scattering mechanism and the two smaller eigenvalues contain mainly noise which can yield any value for the anisotropy, without physical meaning [62]. The anisotropy should thus be used with caution.

The result of taking the anisotropy into account is shown in fig. 6.11(right). Apparently the introduction of the anisotropy permits a better classification of the forests. This is not surprising as in the forests more scattering mechanisms can be expected than in fields which results in a lower anisotropy.
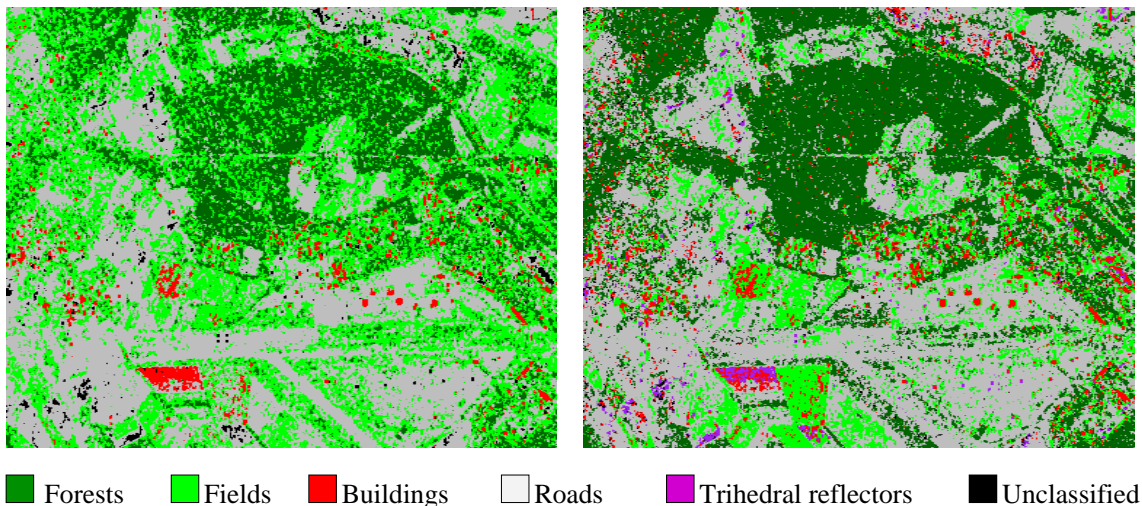

■ Forests   ■ Fields   ■ Buildings   □ Roads   ■ Trihedral reflectors   ■ Unclassified

Figure 6.11: Results for H/α (left) and $anisotropy/H/\alpha$ (Right)

We saw that at very low entropy, the anisotropy is a noisy parameter that should not be used in the classification. Lets now look at the behaviour of the entropy for smooth surfaces. If a surface is very smooth in comparison with the radar wavelength, most of

the radar energy is scattered away from the radar and what is seen in the image is mainly (additive) noise. The classification so far takes no account of the actual returned energy. The additive noise will result in an increase of entropy. Hellmann [63, 60] also uses the value of the first eigenvalue as a parameter for the classification. Although; this parameter is not normalised, it is possible to attribute some boundaries to it for the fuzzy membership functions. Note that the eigenvalue, as well as the values of the other parameters discussed so far are all roll-invariant [61]. Incorporating λ_1 into our fuzzy classification scheme yields the result in fig. 6.12. In that figure, the results are shown with and without the anisotropy.
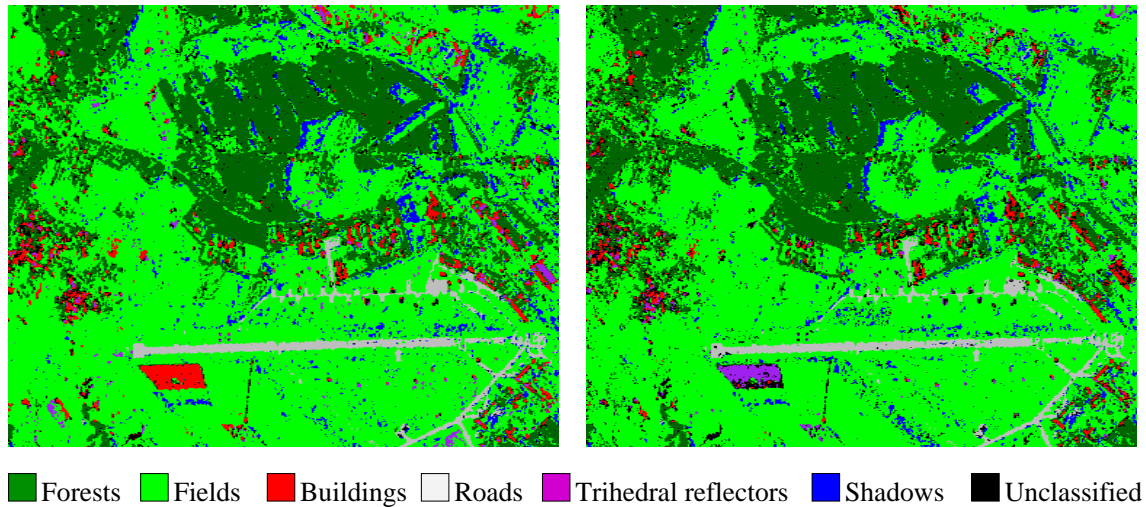

■ Forests ■ Fields ■ Buildings □ Roads ■ Trihedral reflectors ■ Shadows ■ Unclassified

Figure 6.12: Results for $H/\alpha/\lambda_1$ and *Anisotropy*$/H/\alpha/\lambda_1$ space

Introducing λ_1 allows thus to distinguish the runway and main taxiways of the airfield from the surrounding grass. Even if the anisotropy is not used,λ_1 allows to clearly delimit the forests. It also allows to specifically find triheders and shadow regions. Without this parameter, shadow regions can not be distinguished from forest; they also have a low anisotropy and very high entropy (because they represent purely additive noise).

If an interferometric set of polarimetric SAR images is available, one way of taking into account the extra information is by using the interferometric coherence [64]. The interferometric coherence Γ is defined as the absolute value of the normalised complex correlation coefficient:

$$\Gamma = \frac{||<S_{xy,1}S^*_{xy,2}>||}{\sqrt{<S_{xy,1}S^*_{xy,1}><S_{xy,2}S^*_{xy,2}>}}, \tag{6.25}$$

in which $<>$ denotes a spatial average (as always to reduce the influence of speckle), xy is the polarisation (i.e. HH,HV or VV) and the indices 1 and 2 denote the two interferometric images.

The results of the fuzzy classification using this extra parameter are presented in figs. 6.13 and 6.14.
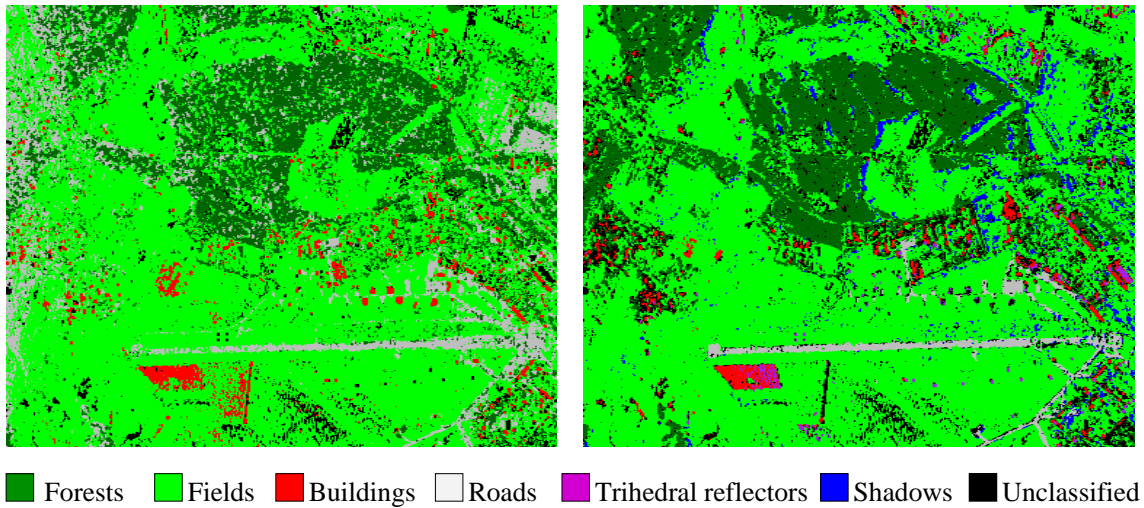
■ Forests ■ Fields ■ Buildings □ Roads ■ Trihedral reflectors ■ Shadows ■ Unclassified

Figure 6.13: Results for $H/\alpha/coherence$ and $H/\alpha/\lambda_1/coherence$

■ Forests
■ Fields
■ Buildings
□ Roads
■ Trihedral reflectors
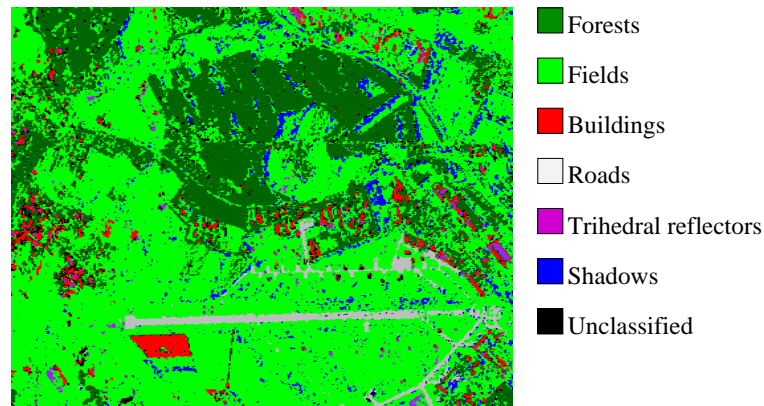■ Shadows
■ Unclassified

Figure 6.14: Results for $A/H/\alpha/\lambda_1/coherence$

6.3 Lessons Learned

For segmentation of large regions the existing Merge Using Moments method was extended to the multi-variate case. The threshold for merging neighbouring regions was made adaptive on the size of the regions to be merged. Because the difference in spatial correlation in range and azimuth influences the false alarm rate for a given threshold, ideally the threshold should take into account the form of the region as well.

For image classification we investigated the use of three existing polarimetric decomposition methods. The aim was to detect forests and built-up areas because we need them for image registration. The decomposition method of Van Zyl and Freeman can not distinguish built-up areas from forests. With the Cloude decomposition it is possible to detect the forests. If supplementary features such as the value of the backscattering

coefficient (and the interferometric coherence) are also used, it is possible to detect some double-bounce scatterers, shadow areas and roads as well. However, it is not possible to detect built-up areas directly. All three methods do detect some double-bounce reflections within villages but these are also found in some locations in the forests. It is thus not possible to delimit the built-up areas. A possible solution is to investigate the specific characteristics of built-up areas in polarimetric SAR images and to use these to develop a specific detector for such areas. This idea is explored in the next chapter. The results of such a detector will complete the results provided by the decomposition methods.